

# Analysis and Comparison of new Downlink Technologies for Earth Observation Satellites

Hennes HENNIGER, Stefan SEYFARTH, Erhard DIETRICH

German Aerospace Center (DLR), German Remote Sensing Data Center (DFD)  
Muenchener Str. 20, 82234 Wessling, Germany

hennes.henniger@dlr.de, stefan.seyfarth@dlr.de, erhard.diedrich@dlr.de

Manuscript received March 1, 2016

**Abstract.** *New generation of Earth observation sensors are creating an increasing amount of data which has to be delivered from space-to-ground. Additionally, many applications require timely availability of this sensor data. As new link technologies have been made available in the last years and data rate requirements are still increasing a revise of the conventional direct-downlink technology at X-band frequencies is essential. This work aims in a trade-off of the available direct-downlink technologies for satellites in low, polar orbits. Generally, there are two approaches to fulfill the requirement of timely delivery of a huge amount of data from space-to-ground. This is either increasing space-to-ground contact time resulting in a more complex ground station network or increasing carrier frequency whereas link reliability is limited by atmospheric effects. In this work different approaches like using  $K_a$ -band or utilizing ground station network with additional locations are compared against each other.*

## Keywords

Earth observation, downlink technologies, space mission design, space-to-ground link

## 1. Introduction

Considering the current mission studies being made in the design of Earth observation missions, one must address the implications of finding new solutions which would maximize the performance of the space-to-ground payload data transfer interface.

The history of Earth observation missions is showing up with an ever increased total daily data volume. Starting from e.g. the ERS-1 and ERS-2 missions of the European Space Agency or the US Landsat missions up to the currently operational German TerraSAR-X and TanDEM-X missions the daily data volume grew up to some thousands of Gbit a day per mission. Reaching the order of magnitude of above 8 Tbit/d with the first Copernicus satellites (e.g. Sentinel 1A)

the next generation missions will reach the multiple tens of Tbit range of daily data volume. The upcoming mission concepts of large constellations of small or micro satellites are not taken into account here. Along with this increasing daily data volume the overall volume of archived data in the same time period shows up with an exponential growth. These figures clearly indicate an increasing demand in downlink capacity. This capacity requirement can either be fulfilled by increasing the contact time of the spacecraft (S/C) to the ground station (G/S) network. That means expanding the ground station network (GSN) by adding more and more G/Ss. Nevertheless, this is somehow limited by commercial aspects as building G/Ss and connecting them to processing centers with high capacity terrestrial data transportation networks can also become costly. Therefore, also the increase in space-to-ground data rate is a promising solution.

Under certain constraints also a GEO-relay approach is a valuable direct space-to-ground link alternative. GEO-relay satellite approaches for polar orbiting satellites data download is addressed in detail in [1] and shall not be repeated in this work. [1] can be summarized comparing only service costs nowadays the traditional direct downlink concept outperforms the GEO-relay scenario on financial aspects. Additionally, GEO-relay does not scale easily with an increased number of Earth observation satellites using GEO-relay. So it can be expected that with a large number of S/Cs which are designed to connect to ground via GEO-relay the downlink capacity is also very limited.

In this work the authors present study findings regarding particular aspects of the downlink architecture and potential design trade-offs. The discussion centers on a trade-off on usable downlink frequency bands as a key driver to provide necessary downlink capacity fulfilling demands of future Earth observation missions. The remainder of this paper is organized as follows: In Sec. 2 the layout of the GSN for polar orbiting Earth observation satellites is discussed. Aspects like total number of G/Ss necessary as well as spatial distribution of the G/Ss are addressed. The discussion aims in proposing solutions to fulfill high downlink capacity needs. Orbit simulations are presented in order to verify the thesis made. In Sec. 3 a direct trade-off between  $K_a$ -band and X-

band space-to-ground carrier frequencies links is presented. Physical impacts and their difference between the two mentioned frequency bands are investigated in depth resulting in relative measures to compare both frequency bands. The paper concludes with Sec. 4.

## 2. Spacecraft Matched Ground Segment Design

This section includes an example mission concept and aims to analyze the necessary space-to-ground downlink data rate or carrier frequency band respectively. The data rate mainly depends on the possible space-to-ground contact time as well as on the payload data volume which is required to be delivered from space-to-ground. The trade-off between contact time meaning number of G/Ss which serve the mission and frequency band is shown in Sec. 2.2. An exemplary future mission orbit which is used for concrete analysis is introduced next. This exemplary orbit is used for further detailed analysis in Sec. 2.2.2.

### 2.1 Definition of Exemplary Mission

We present here in this section the trajectory design for an exemplary future Earth observation mission.

The orbit plane of Earth observation satellites is in most times required to maintain a fixed angle with respect to the sun in order to ensure adequate illumination of the imaging area for optical sensors or to ensure sufficient radiation on solar panels to supply sensor electronics. That determines the trajectory of the S/C to be a polar orbiting, sun-synchronous low Earth orbit (LEO). The orbit cycle gives the time when the ground track of the S/C is repeated. For our reference orbit the orbit duration is 96 min, which leads to a number of 119 orbits per cycle period. The orbit altitude is always a trade-off between sensor resolution which is indirect proportional to the orbit altitude and the atmospheric drag which increases with lowering the orbit. Typical orbit altitudes are in the range of 500 km and 800 km, e.g. TerraSAR-X: 514 km, WorldView-3: 617 km, or Radarsat-2: 798 km. We have arbitrarily chosen an orbit altitude of 600 km for further analysis.

For the sensor instrument of our reference mission we assume a synthetic aperture radar (SAR) which generates typically even more data than an optical instrument. Based on several mission studies for missions which shall be launched in the early 2020s it is up to the author's knowledge that a data volume of 40 Tbit/d is a typical value which shall be assumed here as a minimum requirement. This is by far not the maximum but a good estimate. The volume can easily double for certain instruments.

In general one can think these 40 Tbit/d which are collected in Earth observation instrument operation bursts

can continuously downlinked to Earth which would give us a downlink data rate of 462 Mbit/s. Nevertheless, this is not true because on the one hand there is not always a G/S in the visibility of the S/C, especially not in the mid-latitude regions where a G/S has visibility only to a narrow field of longitude variations. The limited visibility of G/Ss increases the need for higher downlink data rates. This data rate aspect will be addressed in the next section more in detail.

### 2.2 Layout of the Ground Station Network

In this section the number of necessary G/Ss will be analyzed while the number of G/Ss depends on boundary conditions like possible downlink data rates in different radio frequency bands. First, a brief review of the state of the art downlink technology is provided in Sec. 2.2.1. Second, in Sec. 2.2.2 the necessary number of G/Ss and the spatial distribution of G/S on the Earth are investigated.

#### 2.2.1 Downlink Frequency Band

Nowadays, radio frequency (RF) simplex links are used for space-to-ground payload data download. Most often the very robust low order Quadrature Phase Shift Keying (QPSK) modulation scheme is applied to a carrier. Carrier frequencies are typically in the frequency range of 8.025 to 8.400 GHz. This frequency range is also referred to as X-band. According to the regulations of the International Telecommunications Union (ITU) only 375 MHz bandwidth is available per mission in the X-band [2]. Typical possible user data rates end up in between several tens of Megabit per second up to 500 Mbit/s per channel. For example WorldView-2 uses the full bandwidth in order to downlink with 400 Mbit/s per polarization whereas TerraSAR-X achieves 300 Mbit/s applying QPSK within 275 MHz. Using orthogonal channels (e.g. left-hand circular and right-hand circular or dual carrier communication) one can double the effective downlink data rate. From design studies for future missions it is known that user data rates up to 936 Mbit/s per satellite are possible within the X-band. It can be assumed that the limitations in X-band are around 1 Gbit/s user data rate. User data rate means that the data rate on the channel is some percent larger due to redundant information added by forward error correction. The goal of forward error correction is to get closer to the theoretical maximum information transfer rate of a channel. This maximum of 1 Gbit/s user data rate is driven by the available 375 MHz of bandwidth and the acceptable bit error probability but also by technical means like effort to spend for space and ground antenna systems and available transmit power to close the link budget.

To fulfill the requirements of increased payload data downlink user data rates the ITU has allocated the 25.5 to 27.0 GHz band (commonly referred to as the  $K_a$ -band) [2]. The maximum available bandwidth per satellite is 1500 MHz. For data rates above 1 Gbit/s, even the  $K_a$ -band will only be able to support a few missions without generating interference between different S/Cs competing for the same

spectrum. This drives the need for higher order modulation schemes in order to offer better bandwidth efficiency in terms of bit/s/Hz. Complex modulation schemes come with the drawback of decreased robustness against atmospheric effects. Additionally, the shorter wavelengths of  $K_a$ -band signals undergo a different interaction with atmospheric particles than X-band signals. These differences will be analyzed in depth in Sec. 3. In  $K_a$ -band downlink systems are known which can provide up to 3.5 Gbit/s user data rate using two orthogonal channels. These systems are using Adaptive Coding and Modulation (ACM) with an order of 17 [3].

By extending carrier frequencies to the optical spectrum theoretically a remarkable increase in downlink data rate is possible. Free-space optical communications (FSO) has become increasingly interesting as technology to provide high bandwidth for space-to-ground links, whereas nowadays almost no regulative constraints apply to optical frequencies. One of the biggest challenges for FSO links is the signal disturbance accumulated during propagation through the different layers of the atmosphere. Optical systems suffer mainly from index-of-refraction turbulence which leads to a variation of the optical propagation behavior through turbulent mixing of air-cells with different refractive indices. Additionally, the system suffers from significant quasi constant atmospheric losses like atmospheric extinction, e.g. caused by clouds, fog or snow and rain and varying during the connection time between the S/C and the G/S. All these effects can lead to great dynamics of the received signal and thus degradation of link performance during a space-to-ground link [4], [5]. Furthermore, optical space-to-ground links suffer from limited availability due to cloud blockage. Nevertheless, LEO-to-ground links have been performed to proof the concept of optical downlinks, e.g. downlink data rates of 5.625 Gbit/s have been demonstrated [6] [7]. Comparing the currently optically achieved data rates with the possibilities in  $K_a$ -band it has to be concluded that optical systems can not outperform significantly. Taking into account also the drawbacks caused by the atmospheric propagation through the atmosphere optical systems are nowadays not an alternative for space-to-ground links. Optical links have their advantage in space-to-space links where no atmosphere is disturbing and optical systems can gain from their narrow beams.

Concluding the section the Tab. 1 summarizes the discussion above and provides a rough overview about the possibilities and challenges of the different frequency bands discussed for space-to-ground payload data downlinks.

	X-band	$K_a$ -band	FSO
$DR_{max}$	1.0 Gbit/s	3.0 Gbit/s	5.625 Gbit/s
$BW$	375 MHz	1500 MHz	no regulations
atmospheric degradation	negligible	high below 5° elevation	critical

**Tab. 1.** Comparison of frequency bands for LEO downlinks: maximum technical feasible data rates  $DR_{max}$ , bandwidth  $BW$  for Earth exploration services according ITU.

### 2.2.2 Number and Spatial Distribution of Ground Stations

In the following three different exemplary GSN scenarios are generated with the goal to demonstrate the downlink capacity available to serve the mission with the orbit parameters as defined in Sec. 2.1.

Out of already existing and well known G/S sites several G/S locations are selected as follows: As orbits from Earth observation missions always cross the polar regions at any orbit an Arctic and Antarctic G/S sites are an absolute requirement to maximize the number of possible passes. Polar G/Ss can assure access to the S/C twice per orbit and thus permitting data download at least approximately every 45 min. This timing can be important for near real time applications needing images shortly after imaging. It is also important to empty the S/C memory on a regularly basis. In all three scenarios we select at least two G/Ss in the Arctic and one or two Antarctic G/Ss. This selection is enforced by the argument that forwarding received data from the G/S to the processing centers must be cost effective. That means available terrestrial ground communication infrastructure is a driving factor.

Communication infrastructure in Antarctica is challenging. The Norwegian Troll G/S and the German Antarctic Receiving Station (GARS) O’Higgins are considered. Whereas in case of the Troll G/S a dedicated  $K_a$ -band transponder on a GEO-relay communication satellite is used, similar communications solutions for GARS O’Higgins are under investigation and currently a much poorer broadband communication is in operations only. Thus Troll has currently much better capability for data repatriation while GARS O’Higgins is somehow superior with respect to the orbit complement to the north polar stations like Svalbard (or Kiruna) and Inuvik. Therefore, first Troll only is selected as G/S in Antarctica and for the more challenging scenarios both G/Ss are selected. Communication infrastructure in the Arctic is much better: Inuvik (Canada), Svalbard as well as Tromsø (Norway) and Kiruna (Sweden) are known to be connected to the international terrestrial fiber communication network. As a combination of Inuvik and Kiruna can provide a very long contact time to the S/C without having any overlap between the coverages of the G/Ss these both are selected in the Arctic region.

GARS O’Higgins has the advantage of being located in the center of a relatively high density of logistic operations around the Antarctic peninsula. That makes GARS O’Higgins preferable to provide near-real-time (NRT) support with products generated out of received Earth observation data to these logistic operations [8]. These services are focused on but not restricted to maritime produces, e.g. NRT-ice monitoring products.

For all G/Ss an elevation mask of 5° and no keyhole is assumed. That means G/Ss which are equipped with full-motion antenna systems can receive data from the S/C whenever the S/C can be seen from the G/S under elevation angles

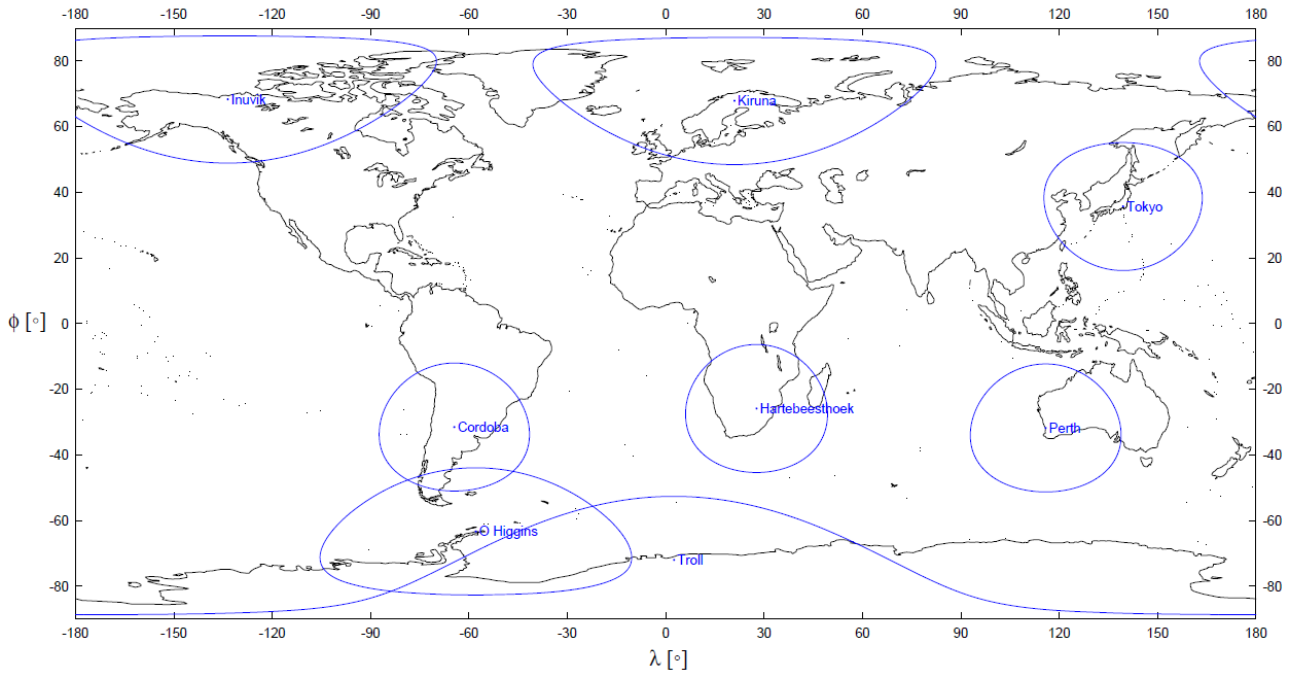


**Fig. 1.** International GSN including coverage circles for the 600 km altitude satellite orbit as defined in Sec. 2.1 and elevation mask of  $>5^\circ$ .

	Downlink Technology				X-band	$K_a$ -band	$K_a$ -band
	Latitude	Longitude	contact time		1 Gbit/s	3 Gbit/s	3 Gbit/s
G/S	$\phi$ [°]	$\lambda$ [°]	[s] per cycle	% of cycle	Scenario 1	Scenario 2	Scenario 3
Svalbard	78.233	15.382	59052	9			
Tromsø	69.660	18.941	45297	7			
Inuvik	68.318	-133.530	43804	6	x	x	x
Kiruna	67.858	20.967	43191	6	x	x	x
Troll	-72.012	2.538	47846	7	x		x
O'Higgins	-63.321	-57.901	36594	5		x	x
Neustrelitz	53.330	13.000	23254	3			
Weilheim	47.880	11.085	20226	3			
Fucino	41.980	13.602	17914	3			
Matera	40.650	16.704	17495	3			
Tokyo	35.701	139.492	16275	2	x		x
Perth	-31.802	115.885	15464	2	x		x
Cordoba	-31.524	-64.464	15371	2	x		x
Hartebeesthoek	-25.887	27.713	14378	2	x		x
S/C TX on-time [% of cycle]					28	18	34
Data volume [Tbit/cycle]					196.3	370.8	698.8
Data volume [Tbit/d]					24.5	46.3	87.3

**Tab. 2.** Data volume per day for selected downlink scenarios. The calculation is based on the exemplary mission defined in Sec. 2.1 and applied to a J2 Perturbation (first-order) propagator which accounts for secular variations in the orbit elements due to Earth oblateness. For all G/Ss a minimum elevation angle of  $5^\circ$  is assumed.

greater than or equal  $5^\circ$ . Fig. 1 presents the coverage area circles of all G/Ss. A 600 km altitude satellite orbit was assumed to generate the coverage circle plots. A list of these G/Ss is also provided in Tab. 2. The selection of G/Ss sites which we have chosen for investigations is arbitrarily but orientated on already existing sites.

Based on orbit analysis and numerically simulating one orbit cycle the G/S contact times can be calculated and summarized. For the results provided here a J2 Perturbation propagator which accounts for secular variations in the orbit elements due to Earth oblateness was used. The propagator does not consider atmospheric drag or solar or lunar gravitational forces. The contact times for our selection of G/Ss are shown in Tab. 2. It shall be mentioned that the contact time can vary over the days but they are periodic with the orbit cycle.

In Tab. 2 three different scenarios are defined to compare different ground segment setups. The scenarios are defined as follows:

In *Scenario 1* additionally to the polar G/Ss as much as possible high- and mid-latitude G/Ss are selected in order to maximize downlink time per cycle (cf. Tab. 2). State of the art X-band communication technology providing 1 Gbit/s is assumed. It can be clearly seen that polar G/Ss provide a great percentage of downlink time while adding mid-latitude G/Ss to the GSN shows only a minor increase in downlink time per cycle. This scenario points out clearly the limitations in downlink capacity when using X-band technology: even a great effort in a large GSN cannot provide more than 24.5 Tbit/d. This number equals 3.1 TB/d. A similar number of 3.7 TB/d is given in [1] for a similar G/S network. This verifies the analysis.

In *Scenario 2* (cf. Tab. 2)  $K_a$ -band downlink is used instead of X-band technology providing 3 Gbit/s. A minimum effort is spent for the GSN focusing on polar G/Ss. A selection without overlap in the coverage circles of the G/Ss which can provide long contact times per cycle is selected. Additionally, a focus on northern polar G/Ss is set as the connectivity to ground communication network is better in the north. This all results in a downlink capacity of 46.3 Tbit/d. This is almost twice the value experienced in *Scenario 1*. This is enabled by high downlink data rates provided by  $K_a$ -band.

In *Scenario 3* (cf. Tab. 2) somehow the maximum technical feasible data downlink capacity is evaluated by using  $K_a$ -band in combination with a large set of polar and mid-latitude G/Ss. This ends up with 87.3 Tbit/d. Again almost twice of what *Scenario 2* can provide. It shall be noted that the Troll and O'Higgins G/S have some overlap in coverage circles. That means in reality the total possible data downlink capacity is a little bit less than reported here because only one G/S can receive data from the S/C at a time.

Summarizing what has been shown above it can be noted that the increasing need of downlink capacity can only be provided by  $K_a$ -band technology. On the example of *Sc-*

*nario 1* it has been shown that the improvement by adding more and more mid-latitude G/Ss is negligible as it does not enable the use of X-band technology to provide a downlink capacity sufficient for future missions. It still requires  $K_a$ -band communications.  $K_a$ -band communications faces several challenges compared to the state of the art X-band downlinks. The trade-off between these downlink frequency bands is discussed in detail in the next section.

### 3. Trade-off Between X- and $K_a$ -Band Frequencies for High Rate LEO Downlinks

#### 3.1 Free-Space Loss

In this section, the impact of increasing carrier frequency from X- to  $K_a$ -band on the free-space loss is investigated. The free-space loss  $L_{\text{FSL}}$  in decibel (dB) can be derived by the Friis transmission formula and results in [9]

$$L_{\text{FSL}}|_{\text{dB}} = 92.45 \text{ dB} + 20 \lg f|_{\text{GHz}} + 20 \lg d|_{\text{km}} \quad (1)$$

with  $d$  being the distance between G/S and S/C and  $f$  being the carrier frequency. As can be seen from (1), the increase in signal loss when changing carrier frequency from 8 GHz to 27 GHz is 10.5 dB. Additionally to the free-space loss, atmospheric effects can generate losses which are discussed in the following sections.

#### 3.2 Rain Loss

Scattering and absorption are essential interactions between an electromagnetic wave and a raindrop, respectively a rain field. On a downlink path, these interactions result in a loss of received signal power and degradation of signal-to-noise ratio. In this chapter, we will discuss the rain loss at low elevation space-to-ground paths when increasing the carrier frequency from X- to  $K_a$ -band. Firstly, we will discuss rain loss using a time variant rainfall rate profile. Secondly, we will introduce a point-rainfall rate in terms of rain loss estimation. Finally, we will define a relative rain loss.

##### 3.2.1 Time Variant Rainfall Rate Profile

Assume a rain field with time variant rainfall rate  $R(x, t)$  and an electromagnetic wave traveling along the slant path  $x$  into the rain field at  $x_r$  to a G/S located at  $x_0$ . For rain loss investigation, only the part of the signal path which is affected by rain ( $R > 0$ ) is of interest. In Fig. 2 the concept of a time variant rainfall rate profile  $R(x, t)$  along slant path  $x$  is shown.

The specific rain loss  $\gamma_R(x, t)$  describes the loss in signal power per km within a rain field ( $x_0 \leq x \leq x_r$ ) of rainfall rate  $R(x, t)$  by the power-law relationship [10]

$$\gamma_R(x, t)|_{\text{dB/km}} = k \cdot R(x, t)|_{\text{mm/h}}^\alpha \quad (2)$$

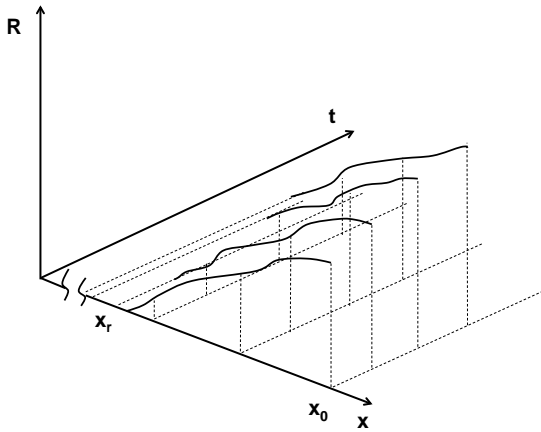


**Fig. 2.** Time variant rainfall rate  $R(x, t)$  along signal path  $x$ . The G/S is located at  $x_0$  and the end of the rain field is  $x_r$ .

In this model,  $k$  and  $\alpha$  are power-law coefficients which were derived from curve fitting of scattering calculations. The power-law coefficients are elevation dependent and slightly polarization-sensitive [10]:

$$k = [k_H + k_V + (k_H - k_V) \cos(\epsilon)^2 \cos 2\tau]/2, \quad (3)$$

$$\alpha = [k_H \alpha_H + k_V \alpha_V + (k_H \alpha_H - k_V \alpha_V) \cos(\epsilon)^2 \cos 2\tau]/2k \quad (4)$$

with  $\epsilon$  being the path elevation angle and  $\tau$  the polarization tilt angle of the propagating beam relative to the horizontal.  $k_H$ ,  $k_V$ ,  $\alpha_H$ , and  $\alpha_V$  are frequency dependent values for horizontal and vertical polarization. In Tab. 3 the coefficients for selected X-band and K<sub>a</sub>-band frequencies are listed.

$f$	8 GHz	12 GHz	18 GHz	27 GHz
$k_H$	0.0041	0.0239	0.07078	0.1884
$k_V$	0.0035	0.0246	0.07708	0.1813
$\alpha_H$	1.3905	1.1825	1.0818	0.9780
$\alpha_V$	1.3797	1.1216	1.0025	0.9349

**Tab. 3.** Vertical and horizontal polarization coefficients for selected frequencies [10].

Due to the asymmetrical shape of a raindrop about the horizontal, the loss in signal power in horizontal polarization differs from the loss in vertical polarization. Since common LEO RF systems are operating with circular polarization  $\tau = 45^\circ$ , one can see from (3) and (4), that  $\gamma_R(x, t)$  becomes independent of elevation angle. Therefore, the specific rain loss of a circular polarized wave at a selected frequency depends only on the time variant rainfall rate profile  $R(x, t)$  along the signal path.

A schematic presentation of downlink path is shown in Fig. 3. Let  $L_R(t)$  be the rain loss,  $(x_r - x_0)$  the slant path distance within the rain field and  $(\tilde{x}_r - x_0)$  the ground projection of the slant path within the rain field:

$$\tilde{x}_r - x_0 = (x_r - x_0) \cdot \cos(\epsilon) \quad (5)$$

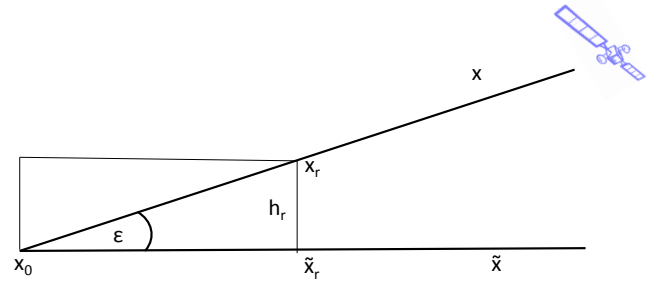


**Fig. 3.** Signal path within a rain field, with  $x$  being the slant path,  $\tilde{x}$  the ground projection of the slant path,  $x_0$  the location of the G/S, and  $h_r$  the height of the rain field.

and for elevation angles  $\epsilon < 10^\circ$

$$\tilde{x}_r - x_0 \approx x_r - x_0, \quad (6)$$

$$\tilde{x}_r \approx x_r. \quad (7)$$

The rain loss  $L_R(t)$  in decibel can be computed by

$$L_R(t)|_{\text{dB}} = \int_{x_r}^{x_0} \gamma_R(x, t) dx \quad (8)$$

$$= \int_{x_r}^{x_0} k \cdot R(x, t)^\alpha dx. \quad (9)$$

For low elevation links, the characteristics of the rainfall rate profile on ground  $\tilde{R}(\tilde{x}, t)$  can be simplified by

$$\int_{\tilde{x}_r}^{x_0} \tilde{R}(\tilde{x}, t) d\tilde{x} \approx \int_{x_r}^{x_0} R(x, t) dx. \quad (10)$$

The simplifications in (7) and (10) show that the rainfall rate  $\tilde{R}$  depends on time  $t$  and position  $\tilde{x}$  but not on the link height above ground.

Therefore, the rain loss  $L_R(t)$  can be computed from the measured or estimated rainfall rate on the ground by

$$L_R(t)|_{\text{dB}} \approx \int_{\tilde{x}_r}^{x_0} k \cdot \tilde{R}(\tilde{x}, t)^\alpha d\tilde{x}. \quad (11)$$

### 3.2.2 Point-Rainfall Rate

The spatial distribution of  $R(x)$  at time  $t_i$  is usually unknown. However, the temporal distribution of  $R(t)$  at the site of interest  $P(\lambda_0, \phi_0)$ , with  $\lambda_0$  being the longitude of the G/S location and  $\phi_0$  being the latitude of the G/S location, can be derived by rainfall rate measurements. For a comparison of loss caused by rain at different sites, it is necessary to provide statements about the period of time for which the rainfall rate and therefore the rain loss exceed given values. In the following the stochastic process  $R(t)$  at  $P(\lambda_0, \phi_0)$  exceeded for 0.01% the time of an average year (i.e. 53 min) is of interest which is equal to a link availability of 99.99%. This leads to  $R_{001}$  and therefore

$$\gamma_{R001}|_{\text{dB/km}} = k \cdot R_{001}|_{\text{mm/h}}^\alpha \quad (12)$$

Site	$\phi_0$ [°]	$\lambda_0$ [°]	$\gamma_{R001}$ (8 GHz)	$\gamma_{R001}$ (27 GHz)
Inuvik	68.318	-133.530	0.1 dB/km	1.6 dB/km
Kiruna	67.858	20.967	0.2 dB/km	3.1 dB/km
Tokyo	35.701	139.492	0.7 dB/km	7.5 dB/km
Hartebeesthoek	-25.887	27.713	0.8 dB/km	8.8 dB/km
Cordoba	-31.524	-64.464	0.5 dB/km	6.2 dB/km
Perth	-31.802	115.885	0.5 dB/km	6.1 dB/km
O'Higgins	-63.321	-57.901	0.2 dB/km	3.1 dB/km
Troll	-72.012	2.538	0.01 dB/km	0.2 dB/km

**Tab. 4.** Specific rain loss exceeded for 0.01% the time of an average year at selected G/S sites.

The rainfall rate  $R_{001}$  varies between different climate zones [11]. In equatorial areas ( $\phi < |23|$ ),  $R_{001}$  can easily reach up to 120 mm/h. Mid-latitude sectors exhibit quite low intensities around 30 mm/h to 60 mm/h. In contrast, polar regions ( $\phi > |68|$ ) indicate very low rain intensities around 15 mm/h.

In Tab. 4 the specific rain loss at 8 GHz and 27 GHz exceeded for 0.01% the time of an average year at selected G/S sites is shown. It can be clearly seen that polar sites such as Inuvik and O'Higgins are favorable in terms of specific rain loss.

The rain loss exceeded for 0.01% the time of an average year can be computed according [12] by

$$L_{R001}|_{\text{dB}} = \gamma_{R001}|_{\text{dB/km}} \cdot x_{R001}|_{\text{km}} \quad (13)$$

with  $x_{R001}$  being the effective path length within a rain field for 0.01% the time of an average year. The effective path length  $x_{R001}$  is a frequency dependent parameter which takes account of the temporal variability of the actual rainfall rate along the path [13].

### 3.2.3 Relative Rain Loss between X- and $K_a$ -Band

Let  $\Delta\gamma_{R001}$  be the relative specific rain loss which occurs when a  $K_a$ -band signal instead of a X-band signal travels through a rain cell. The relative specific rain loss can be computed by

$$\Delta\gamma_{R001} = \gamma_{R001,Ka} - \gamma_{R001,X} \quad (14)$$

$$= k_{Ka} \cdot R_{001}^{\alpha_{Ka}} - k_X \cdot R_{001}^{\alpha_X}. \quad (15)$$

One can see that the relative specific rain loss for circular polarization depends only on frequency and the geographic location. Based on meteorological parameters which were derived from 40 years of data and provided by the European Centre for Medium-Range Weather Forecast (ECM-RWF) ERA-40 database for the prediction of rainfall-rate statistics [11], a map containing the relative specific rain loss  $\Delta\gamma_{R001}$  is derived in Fig. 4. The general decrease in loss when moving away from equatorial areas to polar sites reflects the decrease in point-rainfall rates.

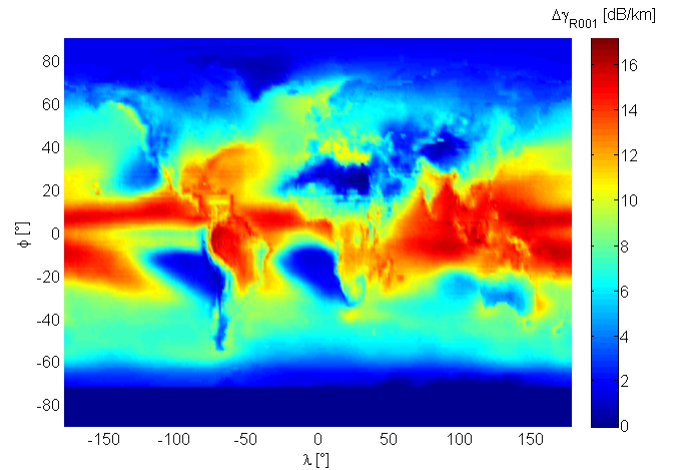


**Fig. 4.** Relative specific rain loss along a constant rainfall rate path exceeded for 0.01% the time of an average year when the carrier frequency increases from 8 GHz up to 27 GHz.

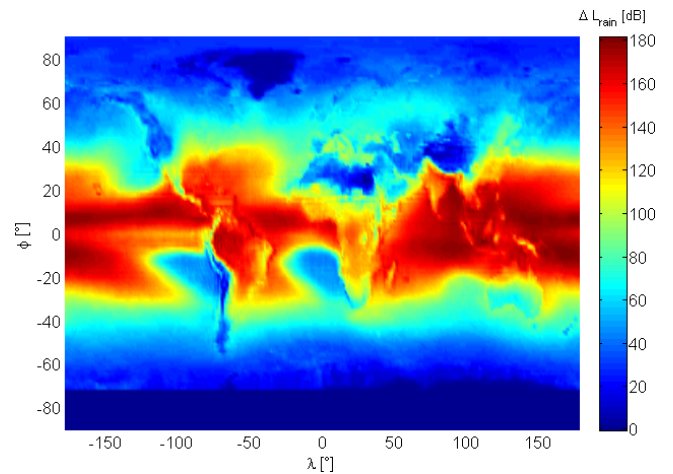


**Fig. 5.** Relative rain loss along a constant rainfall rate path exceeded for 0.01% the time of an average year at  $\epsilon = 5^\circ$  when the carrier frequency increases from 8 GHz up to 27 GHz.

The relative rain loss in decibel can be computed by

$$\Delta L_{\text{rain}} = L_{R001,Ka} - L_{R001,X} \quad (16)$$

$$= \gamma_{R001,Ka} \cdot x_{\text{eff},Ka} - \gamma_{R001,X} \cdot x_{\text{eff},X} \quad (17)$$

$$= \Delta\gamma_{R001} \cdot \Delta x_{\text{eff}} \quad (18)$$

with  $x_{\text{eff},Ka}$  and  $x_{\text{eff},X}$  being the effective path lengths at X- and  $K_a$ -band frequencies and  $\Delta x_{\text{eff}}$  being the difference between these lengths.

Figure 5 illustrates the global distribution of  $\Delta L_{\text{rain}}$  at  $\epsilon = 5^\circ$ . In polar regions the relative loss reaches 60 dB, whereas tropical zones exhibit relative losses up to 180 dB. In Tab. 5 typical values for relative rain loss at various climate zones are shown. The comparison also exhibits a difference between north and south polar sites, due to a slightly higher amount of precipitation per year in the north.

Rain loss is a major loss contributor for space-to-ground links at low elevation angles where the signal travels a long

	$\epsilon$	north polar		equatorial		south polar	
		$\mu$	$\sigma$	$\mu$	$\sigma$	$\mu$	$\sigma$
$\Delta L_{\text{rain}}$ [dB]	3°	38	11	170	40	3.7	9.5
	5°	29	9	140	40	3	7
	7°	23	7	118	29	2	6
	10°	19	6	100	25	1.7	4.5

**Tab. 5.** Mean  $\mu$  and standard deviation  $\sigma$  of relative rain loss exceeded for 0.01% the time of an average year for north polar ( $\phi > 68$ ), equatorial ( $-23 < \phi < 23$ ) and south polar ( $\phi < -68$ ) areas.

distance through the rain field. The specific rain loss is strongly site dependent but exhibits a general decrease when moving away from equatorial areas to polar regions. Since it is not an ever-present loss, the system margin needs to be computed using statistical rainfall data to estimate loss to be exceeded for a given probability. As a result, a large part of cloud loss and atmospheric loss is already included in rain loss estimations for time percentages below 1% [12].

### 3.3 Link Loss Caused by Clouds and Fog

Cloud loss is mainly driven by the liquid water density in cloud or fog  $M$  and the temperature dependent complex dielectric permittivity  $\epsilon_r(f, T)$  of water. The widely used ITU-model [14] is based on Rayleigh approximation and is valid for frequencies below 200 GHz:

$$\gamma_C = K_l \cdot M \quad (19)$$

where

- $\gamma_C$ : specific cloud loss within the cloud [dB/km]
- $K_l$ : specific attenuation coefficient [(dB/km)/(g/m<sup>3</sup>)]
- $M$ : liquid water density in the cloud or fog [g/m<sup>3</sup>].

In a lossy medium, the dielectric permittivity is complex valued, resulting in a temperature and frequency dependency of the specific cloud loss. While the specific loss at X-band frequencies is negligibly small, it can easily reach up to 1 dB/km for 27 GHz K<sub>a</sub>-band systems (cf. Fig. 6).

#### 3.3.1 Time Variant Liquid Water Density Profile

Similar to the approach of the time variant rainfall rate profile, we can define a time variant liquid water density profile  $M(x, t)$ , as shown in Fig. 7, to model cloud loss. The time variant liquid water density profile takes the contributions from the layers of the cloud, which contain water, as well as fog into account.

The mean liquid water density varies with cloud type and can reach values up to 5.0 g/m<sup>3</sup> for cumulonimbus clouds in rare cases [9]. In contrast, cirrus clouds indicate very low water densities about 0.025 g/m<sup>3</sup> (compare Tab. 6). Also the droplet size spectra varies between maritime and continental regions [15].

The water content varies widely with location within a single cloud [9]. The distribution of  $M(x, t)$  along the slant

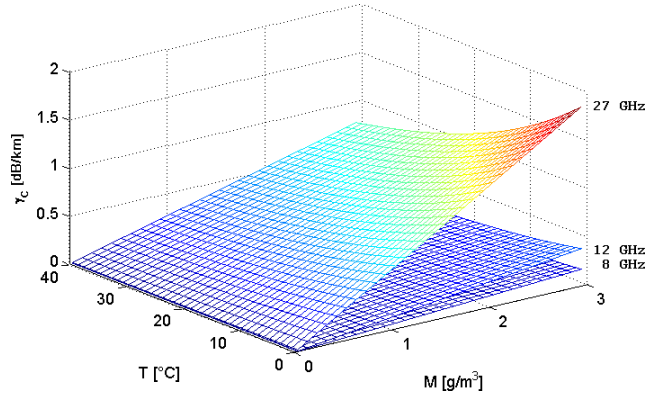


**Fig. 6.** Specific cloud and fog loss for different temperatures and liquid water densities at selected frequencies. For cloud loss assume  $T = 0^\circ\text{C}$ , for fog loss  $T$  is equal to the temperature on ground [9].

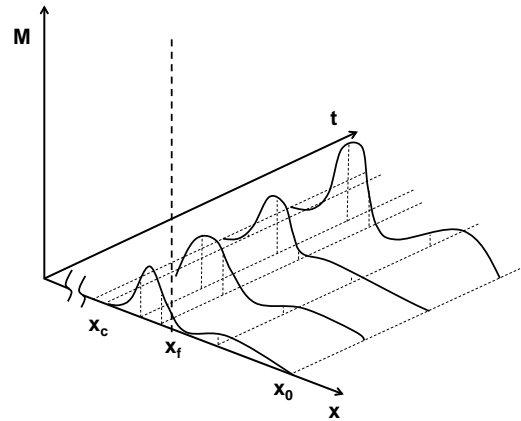


**Fig. 7.** Time variant liquid water density  $M(x, t)$  along signal path  $x$ . The G/S is located at  $x_0$ , the end of the fog field is  $x_f$ , and the end of the cloud is  $x_c$ .

cloud type	$n$ [cm <sup>-3</sup> ]	$r$ [μm]	$M$ [g/m <sup>3</sup> ]
stratus	300	3	0.15
stratocumulus	250	5	0.3
nimbostratus	300	4	0.4
cumulus	300	4	0.5
cumulonimbus	75	5	2.5
cirrus	0.03	250	0.025 <sup>†</sup>
tropical cirrus	0.1	800	0.2 <sup>†</sup>

**Tab. 6.** Typical values of droplet density  $n$ , mean droplet radius  $r$ , and liquid water content (<sup>†</sup> ice water content)  $M$  for different cloud types [15].

path depends strongly on elevation and cloud type. Tropical locations denote far more vertical expanded clouds such as cumulonimbus and cumulus. Stratus and stratocumulus exhibit very low vertical expansion compared to cumulus and can be found at polar and desert sites.

The overall water content  $C(t)$  along the slant path can be computed by

$$C(t) = \int_{x_c}^{x_0} M(x, t) dx \quad (20)$$

$$= \int_{x_c}^{x_f} M_{\text{cloud}}(x, t) dx + \int_{x_f}^{x_0} M_{\text{fog}}(x, t) dx. \quad (21)$$

The resulting cloud loss along a slant path with elevation  $\epsilon \geq 5^\circ$  can be derived by [14]:

$$L_{\text{cloud}}(t)|_{\text{dB}} = \frac{C(t) \cdot K_l}{\sin(\epsilon)}. \quad (22)$$

### 3.3.2 Relative Cloud Loss between X- and $K_a$ -Band

The elevation dependent cloud loss along slant paths exceeded for 0.1% the time of an average year can be predicted using

$$L_{\text{cloud}}|_{\text{dB}} = \frac{C_{01} \cdot K_l}{\sin(\epsilon)} \quad (23)$$

and the relative cloud loss between X- and  $K_a$ -band

$$\Delta L_{\text{cloud}}|_{\text{dB}} = \frac{C_{01}}{\sin(\epsilon)} \cdot (K_{l,Ka} - K_{l,X}) \quad (24)$$

where  $(K_{l,Ka} - K_{l,X})$  represents the carrier adjustment from X- to  $K_a$ -band and  $C_{01}/\sin(\epsilon)$  represents a geographic mapping at elevation  $\epsilon$ .

In Fig. 8 the relative cloud loss at  $\epsilon = 5^\circ$  exceeded for 0.1 % the time of an average year is shown. Especially for tropical regions, where cumulus and cumulonimbus are the most common types of clouds, the loss can be significantly higher than at polar sites. At south polar sites, the relative cloud loss is negligible and can be ignored for S/C downlinks at  $\epsilon \geq 5^\circ$ . Typical loss dimensions are listed in Tab. 7.

At tropical sites the overall water content along a slant path results in a significant decrease in signal power. In contrast, south polar sites reveal the smallest increase in relative cloud loss compared to other climate zones.

### 3.4 Link Loss Caused by Atmospheric Gases

Going into more detail, also under clear-sky conditions we have to expect losses. Atmospheric losses occur as a result of energy absorption by atmospheric gases and aerosols. Under normal atmospheric conditions, only the contributions of oxygen and water vapor are relevant to atmospheric loss on a low elevation slant path. For polar molecules, such as water, the applied RF field causes the charged ends to align with the electric field vector. The continuously occurring realignment with signal frequency results in an absorption loss of RF energy [16]. This process becomes resonant at 22.5 GHz, resulting in an attenuation peak for water vapor.

The link loss caused by atmospheric gases is based on the concept of equivalent heights which assumes an exponential atmosphere specified by a scale height to describe

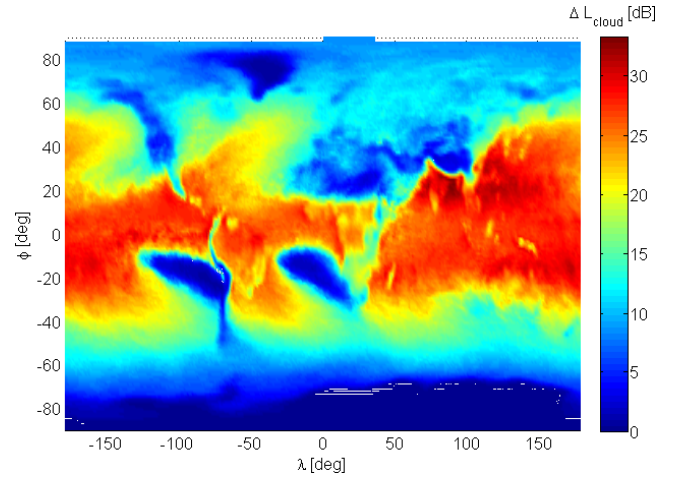


**Fig. 8.** Relative cloud loss exceeded for 0.1% the time of an average year at  $\epsilon = 5^\circ$  when the carrier frequency increases from 8 GHz up to 27 GHz. Blank cells contain areas where no data was available.

	$\epsilon$	north polar		equatorial		south polar	
		$\mu$	$\sigma$	$\mu$	$\sigma$	$\mu$	$\sigma$
$\Delta L_{\text{cloud}} [\text{dB}]$	$5^\circ$	8.6	2	23	6.9	1.3	2
	$7^\circ$	6	1.5	16.6	5	0.9	1.5
	$10^\circ$	4.3	1	11.7	3.4	0.6	1

**Tab. 7.** Mean  $\mu$  and standard deviation  $\sigma$  of relative cloud loss exceeded for 0.1 % the time of an average year for north polar ( $\phi > 68$ ), equatorial ( $-23 < \phi < 23$ ) and south polar ( $\phi < -68$ ) regions.

the decay in density with altitude. According [17] the path attenuation for water vapor  $L_w(t)$  can be obtained by

$$L_w(t)|_{\text{dB}} = \frac{\gamma_w(t)|_{\text{dB/km}} \cdot h_w|_{\text{km}}}{\sin(\epsilon)} \quad 5^\circ < \epsilon < 90^\circ \quad (25)$$

with  $\gamma_w(t)$  being the specific link loss caused by water vapor and  $h_w$  being the equivalent height for water vapor. Correspondingly, the path loss for oxygen  $L_o(t)$  is described by

$$L_o(t)|_{\text{dB}} = \frac{\gamma_o(t)|_{\text{dB/km}} \cdot h_o|_{\text{km}}}{\sin(\epsilon)} \quad 5^\circ < \epsilon < 90^\circ \quad (26)$$

with  $\gamma_o(t)$  being the specific link loss caused by oxygen and  $h_o$  being the equivalent height for oxygen. The overall elevation dependent atmospheric loss is

$$L_{\text{aero}}(t)|_{\text{dB}} = L_w(t) + L_o(t). \quad (27)$$

Fig. 9 shows  $L_o$ ,  $L_w$  and  $L_{\text{aero}}$  at  $\epsilon = 5^\circ$  as functions of frequency under typical mid-latitude atmospheric conditions.

Similar to link losses caused by rain and clouds, the X- $K_a$ -band relative link loss caused by atmospheric gases can be computed by

$$\Delta L_{\text{aero}}|_{\text{dB}} = L_{\text{aero},Ka}|_{\text{dB}} - L_{\text{aero},X}|_{\text{dB}}. \quad (28)$$

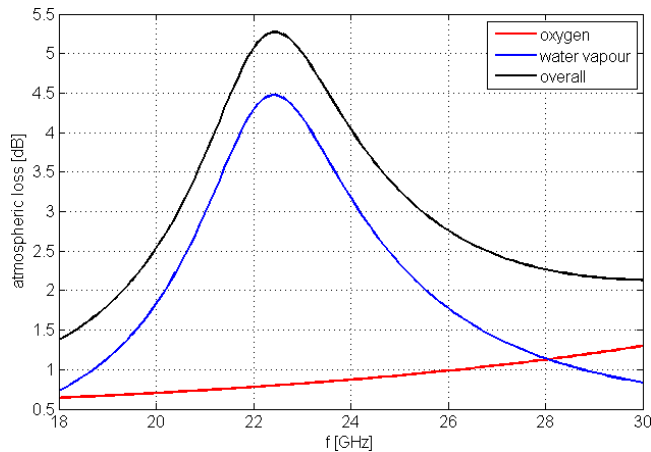


**Fig. 9.**  $L_0$ ,  $L_w$  and  $L_{aero}$  at  $\epsilon = 5^\circ$  as functions of frequency. These losses are valid for typical mid-latitude atmospheric conditions (temperature on ground:  $10.5^\circ\text{C}$ , air pressure on ground:  $1013\text{ hPa}$ , water vapor density:  $7.13\text{ g/m}^3$ ).

The map in Fig. 10 contains the X-/K<sub>a</sub>-band relative atmospheric loss between X- and K<sub>a</sub>-band and had been derived from global datasets of the mean annual ground temperature, mean annual air pressure and mean annual water vapor density provided by ECMRWF.

The loss contributions due to atmospheric gases and aerosols are small compared to precipitation losses. However, comparing X- and K<sub>a</sub>-band losses at different climate zones shows the benefit of dry polar regions against tropical sites. For K<sub>a</sub>-band, the water vapor loss is the dominating factor of the gaseous molecules within the Earth's atmosphere. In X-band the loss is negligibly small and can be ignored.

## 4. Conclusion

The GSN analysis in Sec. 2 clearly show that a development from conventional direct-downlink technology at X-band frequencies to K<sub>a</sub>-band is essential to fulfill downlink capacity needs without extraordinary increase in the number of G/Ss. Additionally, due to the orbit character of low orbiting Earth observation satellites a placement of G/Ss in polar regions is favorable. Sec. 3 proves the applicability of the proposed shift in carrier frequencies from X- to K<sub>a</sub>-band. By relative measures the stronger impact of atmospheric effects on signal propagation at higher K<sub>a</sub>-band frequencies is shown. It is pointed out that with respect to the atmospheric degradations polar G/S sites are favorable. It can be seen that atmospheric degradation on K<sub>a</sub>-band signals are higher than on X-band signals but within a range which is capable by the systems foreseen for the space-to-ground link. All in all K<sub>a</sub>-band shows up to be a feasible and at the same time a rational solution for future high rate data delivery from space-to-ground.

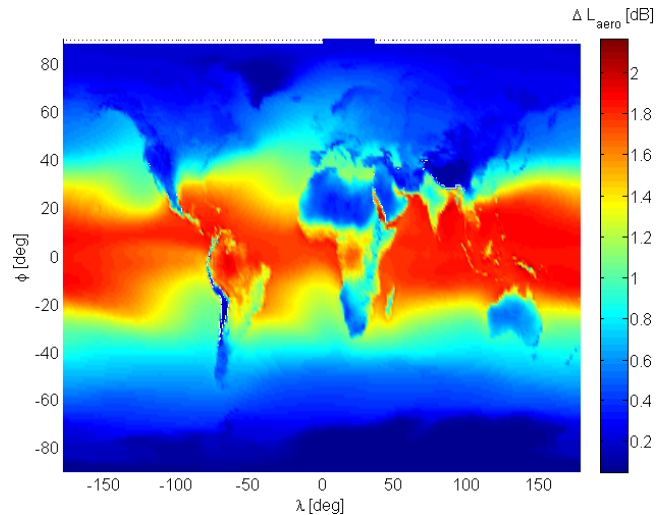


**Fig. 10.** Relative atmospheric loss at  $\epsilon = 5^\circ$  when the carrier frequency increases from 8 GHz up to 27 GHz. Blank cells contain areas where no data was available.

## References

- [1] EILERTSEN, B., HYVÖNEN, P. Ground station networks vs. GEO relay satellite systems for polar orbiting satellites. In *12th International Conference on Space Operations*. Stockholm (Sweden), 2012. DOI: 10.2514/6.2012-1290826
- [2] LEE, D., GRAY, A., KANG, E. et al. A Gigabit-per-second Ka-band demonstration using a reconfigurable FPGA modulator. In *IEEE Aerospace Conference*. Big Sky (MT, USA), 2005, p. 1370–1378. DOI:10.1109/AERO.2005.1559427
- [3] Consultative Committee For Space Data Systems. *Recommended Standard CCSDS 131.2-B-1: Flexible Advanced Coding and Modulation Scheme for High Rate Telemetry Applications*. March 2012.
- [4] HENNIGER, H., WILFERT, O. An introduction to free-space optical communications. *Radioengineering*, 2010, vol. 19, no. 2, p. 203–212.
- [5] HENNIGER, H., LUDWIG, A., HORWATH, J. Performance bounds of DPSK and OOK for low elevation optical LEO downlinks. *Radio-engineering*, 2010, vol. 19, no. 4, p. 586–595.
- [6] GREGORY, M., HEINE, F., KAEMPFNER, H., et al. TESAT laser communication terminal performance results on 5.6 Gbit coherent intersatellite and satellite to ground links. In *International Conference on Space Optics*. Rhodes Island (Greece), 2010.
- [7] GREGORY, M., TROENDLE, D., MUEHLNIKEL, G., et al. Three years coherent space to ground links: Performance results and outlook for the optical ground station equipped with adaptive optics. *SPIE Proceedings*, 2013, vol. 8610. DOI: 10.1117/12.2022253.
- [8] KLÜGEL, T., HÖPPNER, K., FALK, R., et al. Earth and space observation at the German Antarctic receiving station O'Higgins. *Polar Record*, 2015, vol. 51, no. 6, p. 590–610. DOI: 10.1017/S0032247414000540
- [9] IPPOLITO, L. *Satellite Communications Systems Engineering: Atmospheric Effects, Satellite Link Design and System Performance*, 1st ed. Wiley, 2008. ISBN: 978-0-470-72527-6
- [10] International Telecommunication Union. *ITU-R P.878-36: Specific Attenuation Model for Rain for Use in Prediction Methods*, 2005

- [11] International Telecommunication Union. *ITU-R P.873-6: Characteristics of Precipitation for Propagation Modelling*, 2012.
- [12] International Telecommunication Union. *ITU-R P.618-11: Propagation Data and Prediction Methods Required for the Design of Earth-Space Telecommunication Systems*, 2013.
- [13] BARCLAY, L. W. *Propagation of Radiowaves*, 2nd ed. IET, 2008. ISBN: 9780852961025
- [14] International Telecommunication Union. *ITU-R P.840-6: Attenuation Due to Clouds and Fog*, 2013.
- [15] SALBY, M. *Fundamentals of Atmospheric Physics*, 1st ed. Academic Press, 1996. ISBN: 978-0-12-615160-2
- [16] SAUNDERS, S., ZAVALA, A. *Antennas and Propagation for Wireless Communication Systems*, 2<sup>nd</sup> ed. Wiley, 2007. ISBN: 978-0-470-84879-1
- [17] International Telecommunication Union. *ITU-R P.676-10: Attenuation by Atmospheric Gases*, 2013.

### About the Authors ...

**Hennes HENNIGER** was born in 1978 in Berlin, Germany and received his Dipl.-Ing. degree from the University of Applied Sciences, Munich, in 2002, and his Master of Science degree in 2004. He joined the Optical Communications Group of the German Aerospace Center (DLR) in 2001. Since 2010 he is with the German Remote Sensing Data Center working for the department 'International Ground Segment'. He started as coordinator of the TanDEM-X Ground

Station Network and since 2012 Hennes Henniger is head of the team 'Data Acquisition and Reception Systems'. He is station manager of the DLR ground station at the Inuvik Satellite Station Facility.

**Stefan SEYFARTH** was born in 1988 in Friedrichroda, Germany. He received his B.Sc. and M.Sc. from Ilmenau University of Technology, Ilmenau, Germany, in 2013 in electrical engineering with a focus on information and communications technology. As a post-graduate, he joined the German Remote Sensing Data Center at DLR. Since 2014, he is the responsible Operations Manager of the DFD  $K_a$ -band ground station located in Oberpfaffenhofen, Germany. His research interests include  $K_a$ -band communications for Earth observation missions.

**Erhard DIEDRICH** heads the department 'International Ground Segment' of the German Remote Sensing Data Center (DFD) at DLR. This position is held since 2007. From 1983 to 1992, he conducted work in experimental physics at the Max Planck Institute for Physics. After a period as software development and engineering contractor, he joined DLR in 1995 to focus on user information services. In 1998, he became head of the team 'Interoperable Catalog Systems and Internet Gateway Services' at DLR DFD. At that time he was working also on ESA systems for satellite image retrieval and information extraction. In 2002 Dr. Diedrich served as payload ground segment system engineer for TerraSAR-X. Since then he contributed to various mission studies and multi-mission data management projects. Dr. Diedrich holds a PhD in Physics.